Dynamic triggering of an earthquake doublet exposes limitations to rupture forecasting

E. Nissen[1], J. R. Elliott[2], R. A. Sloan[2,3], T. J. Craig[4], G. J. Funning[5], A. Hutko[6], B. E. Parsons[2], T. J. Wright[4]

[1] Department of Geophysics, Colorado School of Mines, 1500 Illinois Street, Golden, CO 80401. USA

[2] COMET, Department of Earth Sciences, University of Oxford, South Parks Road, Oxford OX1 3AN, UK

[3] Department of Geological Sciences, University of Cape Town, Private Bag X3, Rondebosch 7701, South Africa

[4] COMET, School of Earth and Environment, University of Leeds, Leeds LS2 9JT, UK

[4] Department of Earth Sciences, University of California, Riverside, CA 92521, USA

[5] Incorporated Research Institutions for Seismology (IRIS) Data Management Center, 1408 NE 45th St, Suite 201, Seattle, WA 98105, USA

Earthquake hazard assessments and rupture forecasts are based on the potential length of seismic rupture and whether or not slip is arrested at fault segment boundaries. Such forecasts do not generally consider that one earthquake can trigger a second large event, near-instantaneously, at distances greater than a few kilometers. Here we present a geodetic and seismological analysis of a magnitude 7.1 intra-continental earthquake that occurred in Pakistan in 1997. We find that the earthquake, rather than a single event as hitherto assumed, was in fact an earthquake doublet: initial rupture on a shallow, blind

reverse fault was followed just 19 seconds later by a second rupture on a separate reverse fault 50 km away. Slip on the second fault increased the total seismic moment by half, and doubled both the combined event duration and the area of maximum ground shaking. We infer that static Coulomb stresses at the initiation location of the second earthquake were probably reduced as a result of the first. Instead, we suggest that a dynamic triggering mechanism is likely, although the responsible seismic wave phase is unclear. Our results expose a flaw in earthquake rupture forecasts that disregard cascading, multiple-fault ruptures of this type.

Continental earthquakes typically rupture diffuse systems of shallow fault segments, delineated by bends, step-overs, gaps, and terminations. The largest events generally involve slip on multiple segments, and whether or not rupture is arrested by these boundaries can determine the difference between a moderate earthquake and a potentially devastating one. Compilations of historical surface ruptures suggest that boundary offsets of ~5 km are sufficient to halt earthquakes, regardless of the total rupture length[1,2]. This value is incorporated into modern, fault-based earthquake rupture forecasts such as the UCERF3 model for California[3,4], whose goals include anticipating the maximum possible rupture length and magnitude of future earthquakes within known fault systems.

However, if earthquakes could rapidly trigger failure of neighbouring faults or fault segments, at distances larger than ~5 km, then such scenario planning could be missing an important class of cascading, multiple-fault rupture. Here we exploit the combination of spatial

information captured by satellite deformation measurements and timing information of successive fault ruptures from seismology, to reveal how near-instantaneous, probably dynamic triggering may lead to sequential rupture of multiple large earthquakes separated by distances of 10s of kilometers.

The destructive Harnai earthquake occurred on 27 February 1997 at 21:08 UTC (02:08 on 28 February, local time) in the western Sulaiman mountains of Pakistan[5] (Figure 1a). Published source catalogues ascribe it a single, largely (85% – 99%) double-couple focal mechanism with gentle ~N-dipping and steep ~S-dipping nodal planes and a moment magnitude M_w of 7.0 – 7.1 (Supplementary Table 1). The largest catalogued aftershocks include a M_s 6.4 event that struck 22 minutes after the mainshock at 21:30 UTC, and seven further earthquakes of $M > 5.0$ during the next ten months. There were no reports of surface rupturing in any of these events. The Sulaiman mountains lie within the western boundary zone of the India-Eurasia collision where Paleozoic–Paleogene Indian passive margin sediments and Neogene flysch and molasse are folded and thrust over rigid Indian basement[6-9] (inset, Figure 1a; Supplementary Figure 1). Cover thicknesses increase from 8 – 10 km within the low-lying Sibi Trough, south of the range, to 15 – 20 km in the range interior[10-12]. Past instrumental seismicity is dominated by reverse faulting earthquakes with centroid depths of < 10 km, steeply-dipping (30^o – 60^o) nodal planes roughly aligned with local surface folding, and P-axes oriented radially to the curved mountain front as if gravitational forces arising from the topography are important in driving deformation[8,10,13-16].

Surface deformation from InSAR

We mapped the surface deformation in the Harnai earthquake with Interferometric Synthetic Aperture Radar (InSAR), using two images captured on 6 May 1996 and 31 May 1999 by the European Space Agency (ESA) European Resource Satellite (ERS-2) satellite (see Methods). The descending-track satellite line-of-sight has an azimuth of 283^{o} and is inclined at 23^{o} from the vertical at the scene centre. The interferogram (Figure 1b) contains a near-continuous signal in mountainous areas but is decorrelated over most of the Sibi Trough, probably due to agriculture. It contains two distinct fringe ellipses containing displacements toward the satellite, characteristic of slip on buried thrust or reverse faults: one in the scene centre and one in the south-eastern corner of the interferogram. The unwrapped interferogram contains peak displacements of ~60 cm toward the satellite in the central deformation patch and ~50 cm toward the satellite in the south-eastern one (Figure 1c). The south-eastern fringe pattern is partially obscured by an incoherent region where high deformation gradients or mass movements may have caused decorrelation.

To characterize the causative faulting we used elastic dislocation modelling[17,18] guided where possible by independent constraints from seismology (see Methods). The broad fringe ellipse in the scene centre corresponds to slip on a buried, NNE-dipping, shallow-angle (21^{o}) reverse fault (labelled F1 in Figure 1d - e) with a moment magnitude of 7.0. Slip is centred at a depth of ~15 km, consistent with the estimated depth of the basement-sedimentary cover interface in this area[12]. Seismic slip along this interface would rule out the existence of a weak

89 decollement of the kind that underlies the lobate Sulaiman range to the East. Whereas the
90 apex of the Sulaiman range can propagate southwards, facilitated by foreland sediments that
91 are weaker and/or thicker than in neighbouring parts of the Indian plate[8,10,15,16], partial
92 coupling of basement and cover rocks may instead enable the Indian basement to drag the
93 cover northwards, generating the sharp syntaxis around the Sibi Trough (inset, Figure 1a).
94 Similar correspondences between low-angle thrusting and local absence of salt are observed
95 within syntaxes and embayments of other active fold-thrust belts in south Asia[19-21].
96
97 The south-eastern fringe ellipse is caused by slip on another NE-dipping reverse fault (labelled
98 F2 in Figure 1d, e) with a moment magnitude of 6.8. The F2 fault is spatially distinct from F1,
99 being offset southwards, steeper (dip 31^{o}), and shallower (slip is centered at ~9 km, within the
100 sedimentary cover rather than along the basement interface), and there is no indication of any
101 slip connecting the two structures. F2 coseismic uplift is centred along the prominent Tadri
102 anticline (Figure 1a), which may be a fault propagation or fault bend fold controlled by
103 underlying reverse slip.
104
105 We also find that additional reverse slip totalling M_w 6.1 on a third, subsidiary structure
106 (labelled F3 in Figure 1d – e) is required to fit a minor E-W phase discontinuity in the southern
107 part of the central fringe pattern. However, its shallow depth extents (0 – 5 km), elongate
108 dimensions (~20 km) and close spatial correspondence with steep, overturned strata
109 belonging to the southern limb of the Khand Sepal anticline (Figure 1a), suggest that it
110 represents minor bedding plane slip rather than primary earthquake faulting. This

111 deformation resembles after-slip observed along small faults and folds within the hanging-
112 walls of a cluster of larger earthquakes near Sefidabeh in Iran[22], and we suspect that slip
113 associated with model fault F3 also occurred post-seismically.
114
115 **Timing and spacing of seismic slip from arrival times**
116
117 The InSAR models capture the cumulative surface deformation between May 1996 and May
118 1999, but what are the relative contributions from seismic slip in the 27 February 1997
119 earthquake, subsequent aftershocks, and aseismic afterslip? We use seismology to help
120 disentangle the temporal evolution of the signals contained in the interferogram and to
121 provide independent constraints on fault geometry.
122
123 With no local network in place, we are restricted to using Global Seismographic Network
124 seismograms at teleseismic distances, augmented by a few regional stations. Teleseismic
125 broadband, vertical component seismograms (Figure 2a) indicate an abrupt, positive
126 (upwards) arrival that postdates the initial *P*-wave by 16 – 17 seconds at eastern and south-
127 eastern azimuths, by 18 – 20 seconds at northern and north-eastern azimuths, and by 21 – 22
128 seconds at western and north-western azimuths. This azimuthal variation is consistent with a
129 second earthquake that initiates south-east of the first after a delay of ~19 seconds.
130 Henceforth, we refer to these two, distinct events as the Harnai mainshock and +19 second
131 aftershock. It is difficult to identify the second arrival at south-western azimuths, where
132 stations lie close to the SW-dipping auxiliary plane of the InSAR-derived F2 focal sphere (Figure

133 2b); at southern azimuths, stations are located on ocean islands and detection is hampered by
134 oceanic noise.
135
136 We used a multiple-earthquake relocation technique[23,24] to better define the spatial
137 relationship between the epicentres of the mainshock, the +19 second earthquake, and later
138 aftershocks (Figure 2b; see Methods). To calibrate the cluster we exploited the 9 December
139 2008 Ziarat earthquake (M_w 5.7) which occurred in the north-western part of Figure 2b, and
140 whose surface trace is known from InSAR[25-27]. The relocated mainshock epicentre lies at the
141 south-eastern end of the F1 model fault (12 – 14 km south of the published catalogue
142 epicentres), indicating that this fault ruptured first. The epicentral location with respect to the
143 surface deformation implies that mainshock slip then propagated north-westwards along the
144 F1 fault, generating the broad InSAR signal in the centre of the interferograms. The relocated
145 +19 second aftershock epicentre lies ~50 km SE of the mainshock epicentre near the south-
146 eastern end of the F2 fault, at a location in which model slip is restricted to depths of 11 – 17
147 km (Figure 1e). To generate the south-eastern fringe ellipse, the +19 second event must then
148 have ruptured unilaterally towards the NW and from near the bottom upwards.
149
150 Later aftershocks are mostly concentrated within or around the edges of the two main fringe
151 ellipses in the interferograms, though of these only the 27 February 21:30 UTC (M_s 6.4)
152 earthquake is probably large enough to have made a significant contributions to the InSAR
153 deformation. It occurred west of the mainshock hypocentre and may have ruptured or re-
154 ruptured the western part of the F1 slip patch, though we have no independent constraints on

its mechanism. Hypocentre locations and source parameters obtained from modelling long-period teleseismic body-waveforms[19,28] (see Methods) indicate that the 20 March (M_w 5.6), 17 June (M_w 5.0), 24 August (M_w 5.5) and 7 September 1997 (M_w 5.3) aftershocks probably ruptured the down-dip extension of the Harnai mainshock fault plane (Figure 2b). Crucially, the largest catalogued aftershock associated with the south-eastern fringe ellipse is just m_b 5.1 and is thus much too small to have generated the surface deformation associated with the F2 fault (M_w 6.8). This discounts a later aftershock as the cause of the F2 faulting.

Timing, spacing and scaling of seismic slip from back-projections

Seismic back-projections confirm our proposed model of the spatial and temporal relationship between the Harnai mainshock and +19 second aftershock and provide independent seismological evidence in favour of their comparable magnitudes. Using two dense arrays of teleseismic broadband stations centred in Europe (Figure 3a) and North America (Figure 3d), we back-projected coherent *P*-wave energy onto a grid surrounding the source region over a 2 minute period spanning both the mainshock and aftershock [29, 30]. Both back-projections show two distinct peaks in stacked energy, separated by ~18 seconds (Figure 3b, 3e; Supplementary Videos 1, 2). The two peaks have very similar shapes and amplitudes, consistent with comparable moment release in each event. Spatially, the distance and azimuth between the two peaks (31 km and 135^o for the EU back-projection, and 41 km and 146^o for the North American back-projection) are consistent with those separating the InSAR-derived F1 and F2 model fault centre coordinates (49 km and 141^o). This rules out aseismic afterslip as the

177 source of the south-eastern deformation lobe, since this would leave the second, south-
178 eastern peak in seismic radiation completely unaccounted for.
179
180 **Triggering mechanism**
181
182 We have established that the M_w 7.0 Harnai mainshock was followed ~19 seconds later by a
183 M_w 6.8 aftershock, initiating ~50 km to the SE on a spatially distinct fault, but what is the
184 causal relationship between the two earthquakes?
185
186 Firstly, we investigate whether permanent (static) stress changes, imparted by mainshock fault
187 slip upon the surrounding medium once the seismic vibrations have ceased, promoted failure
188 of the aftershock fault, which was presumably also late in its earthquake cycle and critically
189 stressed[31]. We calculated the static Coulomb failure stress change on the aftershock
190 ("receiver") fault caused by slip on the mainshock ("source") fault[32], using the F2 and F1 fault
191 plane parameters, preferred F1 slip distribution, and the same elastic moduli as in our InSAR
192 modelling. Positive Coulomb stresses mean that receiver faults are brought closer to failure
193 (through an increase in shear stresses and/or a decrease in normal stresses), whilst negative
194 Coulomb stresses mean that receiver faults are brought further from failure. Coulomb stresses
195 beneath the aftershock epicentre are negative over its inferred nucleation depth range of 11 –
196 16 km (Figure 4a), with a value of -0.003 MPa at the minimum-misfit hypocentre location itself
197 (Figure 4b).
198

To test the robustness of this result, we repeated the calculation using perturbed source and receiver fault orientations and source slip distributions. Fault strikes, dips and rakes were varied within their formal error bounds, and alternative source fault slip distributions were generated using a range of slip smoothing factors (see Methods and Supplementary Figures 3 – 5). Perturbing either the source fault parameters or slip distribution has no discernible impact on Coulomb stress changes at the aftershock hypocentre. Changing the receiver fault orientation has a larger effect (Supplementary Figure 6), in some instances raising the Coulomb stresses at the aftershock hypocentre to as much as -0.001 MPa, but never to positive values. We also investigated the temporal progression in static stress change on the aftershock fault, by determining static Coulomb stresses generated by each 2-second increment in accumulated F1 slip. Assuming a unilateral F1 rupture propagating from SE to NW at 2.5 km/s (see Methods), we find that Coulomb stress changes at the aftershock hypocentre are negative for the complete duration of F1 rupture (Supplementary Figure 7).

Although certain limitations to our modelling – namely assumptions of planar faults with uniform rake embedded within a uniform elastic half-space – do not permit us to definitively rule out small, positive Coulomb stresses at the location of aftershock initiation, all available evidence therefore suggests that static stresses imparted by mainshock slip on the F1 fault brought the aftershock fault further from failure, not closer. This implies instead that the +19 second aftershock was triggered instead by transient (dynamic) stresses generated by the passing seismic waves.

220 We have no direct constraints on seismic velocities in the sequence of cover rocks above and
221 between the F1 and F2 faults, but we can place conservative bounds of 4 – 7 km/s for average
222 *P*-wave velocities and 2 – 4 km/s for shear and surface wave velocities. This would indicate
223 that the +19 second aftershock initiated several (~6 – 12) seconds after passage of *P*-waves
224 originating at the mainshock hypocentre, at about the same time as the first *S*-wave and
225 emergent surface wave arrivals, and also at around the same time as passage of *P*-waves
226 generated along the north-western F1 fault.
227
228 Of these wave-types, surface waves are most commonly attributed to suspected cases of
229 dynamic triggering due to their larger amplitudes, though body-waves have also been
230 implicated in sequences of deep focus earthquakes[33]. Great earthquakes commonly generate
231 both instantaneous and delayed seismicity at distances of hundreds to thousands of
232 kilometres, where static stress changes are negligible, but these remote aftershocks usually
233 have small magnitudes and often occur in volcanic or geothermal areas with quite different
234 stress and frictional regimes[34-36]. A notable exception was a M_w 6.9 earthquake in Japan that
235 initiated during the passage of surface waves from a M_w 6.6 event in Indonesia, confirming the
236 potential for larger triggered earthquakes in compressive environments[37]. However, whether
237 dynamic triggering also occurs locally (within 1 -2 fault lengths of the triggering event) is still
238 controversial, in part because deconvolving static and transient stress changes within this area
239 is challenging[38-41]. On the one hand, asymmetric aftershock distributions for earthquakes that
240 exhibit a strong rupture directivity[42], and raised aftershock rates for impulsive earthquakes
241 compared to aseismic slip events of the same magnitude[43], both hint at the occurrence of

242 dynamic triggering within the source region. On the other hand, the high amplitude surface
243 waves which impart the largest transient stresses only fully emerge at much larger distances,
244 leading to the very feasibility of dynamic triggering in the near-field (10s of kilometres) being
245 questioned[44].
246
247 Our results indicate that large earthquakes can indeed be triggered at such short distances by
248 transient stresses. However, without better constraints on local seismic velocities or any local
249 stations, and given the likelihood of complex wave interactions within the folded and faulted
250 sedimentary cover, we are unable to determine the wave-type responsible for triggering the
251 +19 second aftershock. It is therefore unclear whether reductions in the normal stresses on
252 the aftershock fault, increases in shearing stresses, changes to pore fluid pressure, or a
253 combination of these factors were responsible. Since static stresses are only fully transmitted
254 once the seismic waves have passed by, we cannot establish what proportion of the (negative)
255 static stress change from F1 slip was felt at the aftershock hypocentre at its origin time, and
256 hence we are unable to place even a lower bound on the (positive) dynamic triggering stress.
257
258 Compilations of historical surface rupture traces have been used to imply that fault segment
259 gaps of ~5 km are sufficient to halt an earthquake rupture[1,2]. This figure is also in broad
260 agreement with numerical earthquake simulations[45]. The notion that segment boundaries
261 larger than 5 km will always arrest slip has since been incorporated into the state-of-the-art
262 UCERF3 rupture forecast models for California[3,4]. Yet a few earthquakes are known to have
263 bridged larger segment boundary distances. Surface traces of the 1932 Chang Ma, China (*M*

~7.6) and 1896 Rikuu, Japan (M ~7.5) reverse faulting earthquakes contain gaps of 10 km and 15 km, respectively[46], whilst the complex M_w 8.6 Indian Ocean intraplate earthquake of 11 April 2012 bridged a gap of ~20 km between subparallel, but separate, strike-slip faults[47]. However, these events are much larger than the Harnai earthquake and it is possible that in each case static stresses were sufficiently large to trigger slip at distances of 10 – 20 km.

The Harnai doublet is unprecedented amongst modern, well-recorded events in involving near-instantaneous triggering at a distance of ~50 km, probably through dynamic rather than static stress transfer. The second earthquake increased the eventual seismic moment by ~50% and doubled both the duration of ground shaking and the area affected by the strongest shaking, illustrating the added danger posed by multi-fault ruptures of this type. The implications of this behaviour are especially relevant to other continental fold-and-thrust belts. Earthquake dimensions in these settings are often obscured due to loss of near-surface slip to folding, limiting the value of historical surface rupture catalogues in anticipating earthquake arrest[45]. Since joint geodetic and seismological analyses are not yet standardized, it is unclear how exceptional triggering of the type observed in the Harnai doublet is. A comparison between geological slip rates and historical earthquake occurrence suggests that multi-segment earthquakes with larger-than-expected magnitudes may be rather frequent amongst the reverse faults of the Los Angeles basin and surroundings[48]. Our results indicate that multiple-fault ruptures (as opposed to merely multiple-segment ones), such as sequential failure of the Sierra Madre and Puente Hills thrusts which are separated by ~20 km, are also mechanically feasible if both systems are critically stressed. Rupture forecast models which

prohibit triggering over such length- and time-scales are likely overly optimistic in anticipating earthquake hazard in areas that contain dense networks of active faults.

Correspondence

Correspondence and requests for materials should be addressed to Edwin Nissen (enissen@mines.edu).

Acknowledgments

This work is supported by the UK Natural Environmental Research Council (NERC) through the Looking Inside the Continents project (NE/K011006/1), the Earthquake without Frontiers project (EwF_NE/J02001X/1_1) and the Centre for the Observation and Modelling of Earthquakes, Volcanoes and Tectonics (COMET). The Incorporated Research Institutions for Seismology (IRIS) Data Management Center is funded through the Seismological Facilities for the Advancement of Geoscience and EarthScope (SAGE) Proposal of the National Science Foundation (EAR-1261681). We are grateful to Eric Bergman for guidance in earthquake relocations, Kevin McMullan and Andrew Rickerby for their assistance with preliminary InSAR and body waveform modelling, and three anonymous reviewers and the editor for comments which helped improve the manuscript.

Author contributions

InSAR analysis and accompanying Coulomb modelling was undertaken by E.N. and J.R.E. Seismological analyses were led by R.A.S. (calibrated multi-event relocation), A.H. (seismic

back-projection) and E.N. (body-waveform modelling). All authors contributed to the interpretation of results and E. N. wrote the manuscript.

Figure Captions

Figure 1 | Tectonic setting and InSAR data and modelling results. (a) Published epicentres and focal mechanisms for the 27 February 1997 earthquake from the USGS National Earthquake Information Center (NEIC, in blue), the International Seismological Centre (ISC, green), the Engdahl, van der Hilst & Bulland catalogue[49] (EHB, magenta), and the Global Centroid Moment Tensor project (GCMT, red). Inset shows tectonic setting with the local motion of India relative to Eurasia[50]. (b) Wrapped and (c) unwrapped interferogram spanning the mainshock and major aftershocks. (d) Model interferogram and faults, with up-dip surface projections marked by dashed lines. (e) Slip view with extents of initial uniform slip model faults indicated by dotted rectangles.

Figure 2 | Seismograms and relocated epicentres. (a) Broadband, vertical component seismograms demonstrating the azimuthal variation in delay between Harnai mainshock and +19 second earthquake P-wave arrivals. LBTB and CRZF are not expected to show impulsive arrivals for the second event. Map shows all stations used in the relocation. (b) Calibrated epicentres for the mainshock, +19 second earthquake, six major aftershocks (stars), and ~150 smaller aftershocks (circles), plotted over the interferogram from Figure 1b. Focal mechanisms from body waveform or InSAR modelling are indicated. To calibrate the cluster we used the

2008 Ziarat earthquake[25-27], assuming that its epicentre (red star) lies at the centre of an InSAR-derived model fault[25] (red line).

Figure 3 | Seismic back-projections. (a) Back-projection array constructed mostly from European seismic stations. (b) Normalized peak beam power stacked over all grid points. (c) Snapshots of coherent energy plotted at 4 second intervals after the initial rupture. For reference, the stars in the 0 second and 20 second plots indicate the relocated epicentres of the mainshock and +19 second earthquake, respectively (Figure 2b), while the small rectangles outline the F1 and F2 model faults (Figure 1d – e). (d) – (f) Back-projection from an array constructed mostly from North American stations, with details as in (a) – (c).

Figure 4 | Coulomb stress changes. (a) Coulomb stress changes caused by slip on NE-dipping source fault F1 at 5 km depth intervals for receiver faults with the same orientation as F2. The +19 second earthquake epicentre is plotted with the 90% confidence ellipse in its relative location (Figure 2b); its hypocentre depth is probably 11 – 17 km. (b) Coulomb stress change resolved onto each receiver fault caused by slip on source fault F1.

Methods

InSAR modelling

We used standard elastic dislocation modelling procedures[17,18] to characterize the faulting observed in the interferogram. Line-of-sight displacements were first resampled using a quadtree algorithm, reducing the size of the dataset whilst concentrating sampling in areas

with high deformation gradients. Representing faults initially as rectangular dislocations buried in an elastic half-space with Lamé parameters $\mu = \lambda = 3.23 \times 10^{10}$ Pa and a Poisson's ratio of 0.25, we used Powell's algorithm with multiple Monte Carlo restarts to obtain the minimum-misfit strike, dip, rake, slip, latitude, longitude, length, and top and bottom depths of each fault, solving simultaneously for a static shift and displacement gradients in the N-S and E-W directions to account for ambiguities in the zero-displacement level and residual orbital phase ramp. Uncertainties in these parameters were then estimated by modelling datasets perturbed by realistic atmospheric noise[17, 18].

The broad fringe ellipse in the scene centre can be reproduced by either of two, 39 km-long, M_w 6.9 model faults (labelled F1), the first which dips 22° NE and projects upwards towards the northern Sibi Trough, and the second which dips 63° SW and projects to the surface at the northern edge of the fringe ellipse. Both involve buried reverse slip centred at 15 – 16 km depth, though slip magnitude is poorly constrained due to a strong trade-off with fault width. The south-eastern deformation pattern can also be reproduced by either of two conjugate, M_w 6.7 – 6.8 reverse faults (labelled F2), one which dips 31° NE and projects up-dip towards the Sibi Trough, the other which dips 57° SW and projects to the surface north of the Tadri anticline. Model interferograms and residual (model minus observed) displacements for all four uniform slip F1 and F2 fault combinations are shown in Supplementary Figure 2, with model parameters given in Supplementary Table 2. However, later we will show that only the NE-dipping F1 and F2 model faults are consistent with teleseismic body-waveform analysis and

epicentral relocations. Parameter trade-offs and errors for these NE-dipping model faults are shown in Supplementary Figures 3 and 4.

To explore the slip patterns in more detail, we extended each model fault by a few kilometres beyond their uniform slip bounds, and solved for the distribution of slip over these surfaces using a Laplacian smoothing criterion to ensure realistic slip gradients[17,18]. Fault rakes were fixed to their uniform slip values, reflecting the single available look direction, and a non-negative least squares algorithm was used to prevent retrograde displacements. The trade-off between slip magnitude and down-dip fault width means that there is no unique solution; instead, a suite of models is generated using a range of smoothing parameters. The preferred model was generated using a scalar smoothing factor of 400 to weight the smoothing[18] (Figure 1d – e; residual displacements shown in Supplementary Figure 5c). The F1 slip patch is ~50 km in length, ~15 km in width (its rather elongate dimensions a robust feature of the inversion), centered at ~15 km depth, and has a M_w of 7.0. The F2 slip patch is ~35 km in length, centred at ~9 km depth, with a M_w of 6.8. Its width is less well-resolved due in part to interferometric decorrelation in its hanging wall. Residuals in the areas between the two faults are negligible, implying an absence of slip in the area between the main F1 and F2 slip patches. We also find that additional reverse slip on a third, subsidiary structure is required to fit a minor, E-W phase discontinuity in the southern part of the central fringe pattern. This M_w 6.1 model fault (labelled F3 in Figure 1d, e) is ~20 km long, dips 18^o N and extends from close to the surface to a depth of ~5 km.

Calibrated earthquake relocations

We used a calibrated earthquake relocation technique[23,24] to relocate the epicentres of the Harnai mainshock and 150 of its aftershocks. Multiple-event relocations exploit the fact that while unknown velocity structure along teleseismic ray paths leads to large uncertainties in absolute hypocentre positioning, phases from clusters of nearby earthquakes sample roughly the same portion of the Earth, permitting much tighter constraints on *relative* hypocentre locations. If the hypocentre of any one (or more) event in the cluster is known independently, the locations for the entire cluster can be calibrated by applying a shift to satisfy these additional constraints. Earthquakes with moderate source dimensions mapped with InSAR are well-suited for calibration purposes[24]. In this instance, we exploit a M_w 5.7 strike-slip earthquake which occurred on 9th December 2008 near Ziarat (NW corner of Figure 1) and which exhibits a clear, well-defined InSAR signal consistent with a vertical or sub-vertical fault with a strike of 242^o - 245^o and a length of 8 – 13 km[25-27]. We take the centre of a uniform slip model fault[25] as its epicentre, resulting in a ~6.5 km uncertainty in the along-strike direction. This earthquake is spatially separated from the main cluster by several tens of kilometres, and lateral variations in the velocity structure within this region may be an additional source of error. To relocate events in the cluster we used the phase arrival times reported in the ISC bulletin. However, the +19 second aftershock was not reported by the ISC and we instead manually picked *P* arrivals from 30 stations at regional and teleseismic distances. We purposely avoided using seismograms at distances <20^o, since many of these contain complex, refracted head waves which make picking the aftershock arrival difficult. It was also difficult to identify this phase in traces from stations to the SW, probably because the *P* arrival is near-

nodal at teleseismic distances in this direction, and also from Indian Ocean stations which are noisy. Consequently the confidence ellipse for this event is elongated in the SSW-NNE direction. During the relocation we excluded the smallest aftershocks for which there were few reported phase arrivals and an insufficient azimuthal coverage to obtain stable epicentres, and we made an empirical estimate of the average reading error for each station-phase pair and 'cleaned' the ISC phase arrival times of clear outliers. The lack of local phase arrival data prevents us from attempting to constrain the hypocentral depths. Our reported locations (Supplementary Table 3) have been determined assuming 15 km hypocentral depths, close to the base of the seismogenic layer in this region[13,15], but using 10 km or 20 km does not significantly change the resulting pattern. Projected onto the NE-dipping F2 model fault plane, the +19 second aftershock hypocentre coincides on a prominent slip patch at 11 – 17 km depth (Supplementary Figure 5a – c). Projected onto the conjugate SW-dipping F2 model fault, the epicentre lies outside the main slip distribution (Supplementary Figure 5d – f), and consequently we are able to discount this candidate fault plane.

Teleseismic body-waveform modelling

Modelling long period teleseismic body waveforms provides independent source parameters for the Harnai mainshock and many of its largest aftershocks. In this approach, earthquakes appear as a point source in space (the 'centroid') and are thus insensitive to short-wavelength variation in fault slip and local velocity structure[28]. By accounting for the separation between direct *P* and *S* arrivals and near-source surface reflections *pP*, *sP* and *sS*, these methods are known to yield more accurate centroid depths than the solutions reported by the GCMT, NEIC

438 or EHB earthquake catalogues, as well as independent estimates of other focal parameters. In
439 some instances teleseismic body waveform modelling can also reveal distinct sub-events and
440 constrain their timing, depths and mechanisms. We used long period (15 – 100 second)
441 seismograms recorded over the distance range 30^{o} – 90^{o} (Supplementary Figure 8). Vertical
442 components were used to model *P, pP* and *sP* phases and transverse component seismograms
443 were used for the *S* and *sS* phases. Without direct measurements of seismic wave velocities in
444 our region of interest, we assumed a half-space with values of 6.0 km/s for the *P*-wave
445 velocity, 3.5 km/s for the *S*-wave velocity and 2.8×10^{3} kg/m^{3} for density, consistent with the
446 elastic half-space structure used in the InSAR modelling. Faster seismic velocities above the
447 earthquake source would result in a shallower centroid depth (and vice versa), whilst the
448 choice of density primarily affects the seismic moment. We used a routine modelling
449 procedure[19,20] that minimizes the misfit between observed and synthetic seismograms to
450 solve for the best-fit strike, dip, rake, scalar moment, centroid depth and source time function
451 of each event. Uncertainties in key parameters of interest were estimated by holding them
452 fixed, inverting for remaining free parameters, and inspecting the degradation in fit between
453 observed and synthetic waveforms[28].
454
455 For the initial earthquake, we obtained a good fit to the first ~20 seconds of the observed
456 waveforms, providing important additional constraints on mainshock mechanism and depth
457 (Figure 2b; Supplementary Table 1 and Supplementary Figure 9), but we could not find a
458 stable two-source solution that would also characterize the +19 second aftershock. The gently
459 NE-dipping mainshock nodal plane strike is relatively poorly constrained at $315^{o}\ ^{+20^{o}}_{-40^{o}}$, trading

off against rake ($140^{o}\ ^{+20^{o}}_{-40^{o}}$) to keep a relatively stable slip vector ($176^{o} \pm 2^{o}$). Within error, this strike thus agrees within that of the NE-dipping candidate F1 fault (290^{o}), and our preferred body-wave solution incorporates the more tightly-constrained InSAR-derived strike as a fixed parameter. The strike of the steeper, ~S-dipping body-waveform model nodal plane is $86^{o}\ ^{+5^{o}}_{-6^{o}}$, in clear disagreement with that of the equivalent candidate F1 fault (107^{o}). On this basis we rule out the SW-dipping fault plane. The NE-dipping nodal plane dips at $14^{o}\ ^{+8^{o}}_{-6^{o}}$, just within error of the InSAR-derived F1 dip of 22^{o}. The centroid depth of 13 km $^{+1\ km}_{-4\ km}$ trades off against the moment of 2.5 $^{+0.9}_{-0.3}$ x 10^{19} Nm, both agreeing to within error with the uniform slip F1 values from initial InSAR modelling. The 20 second duration of the source time function is an especially robust feature of the inversion, closely matching that of the first pulse in the back-projection stacked beam power (Figure 3b, 3f). When combined with the ~50 km F1 fault length and the unilateral (SE to NW) rupture propagation direction, this result yields an estimated rupture velocity of ~2.5 km/s. We attempted to characterize the seismograms with a two-source event, fixing the parameters described above for an initial mainshock and then solving for the source parameters (including the azimuth, distance and time delay) of a sub-event. Though the fit between observed and model seismograms can be improved substantially compared to the single-event model, we find that the sub-event mechanism, depth, and time delay are all highly unstable in this inversion. We are therefore unable to provide seismological constraints on the +19 second aftershock focal mechanism that are independent of the InSAR modelling, as we did for the mainshock.

Source parameters obtained for the largest aftershocks of the Harnai earthquake (Figure 2b; Supplementary Table 4, Supplementary Figures 10 – 14) are similar to those obtained previously using body waveform modelling[15], with discrepancies of at most a few degrees in strike, dip and rake, and up to 2 km in centroid depth. The largest aftershock (4 March 1997, M_w 5.6) was a strike-slip event which occurred SE of the map extents of Figure 2b. The 20 March (M_w 5.6), 17 June (M_w 5.0), 24 August (M_w 5.5) and 7 September 1997 (M_w 5.3) aftershocks have shallow (12^o – 27^o) N- or NNE-dipping nodal planes with slip vectors (170^o – 183^o) that cluster around that of the Harnai mainshock (176^o). Unfortunately seismograms of the 27 February 1997 21:17 UTC (m_b 5.1), 21:30 UTC (M_s 6.4) and 22:41 (m_b 5.2) aftershocks were very noisy, preventing us from obtaining robust solutions for these events.

Data and Code availability

ERS-2 SAR data are copyrighted by the European Space Agency and the raw SLC imagery may be obtained from them upon request. InSAR processing was performed using *ROI_PAC 3.0* software which is freely available from JPL/Caltech (http://www.openchannelfoundation.org/projects/ROI_PAC). Derived interferograms, corresponding metadata and codes for InSAR modelling are available from the authors upon request. Coulomb stress modelling was performed using *Coulomb 3* software which is freely available from the USGS (http://earthquake.usgs.gov/research/software/coulomb/). Seismic arrival time data were obtained from the Bulletin of the International Seismological Centre (http://www.isc.ac.uk/iscbulletin/) and modelled using *mloc* software written by Eric Bergman

(http://www.seismo.com/). Waveform data were accessed through the Incorporated Research Institutions for Seismology (IRIS) Data Management Center (http://ds.iris.edu/ds/nodes/dmc/) and modelled using *MT5* and back-projection codes that are available from the authors upon request.

References

1. Wesnousky, S. G. Predicting the endpoints of earthquake ruptures. *Nature* **444,** 358-360 (2006).

2. Wesnousky, S. G. Displacement and geometrical characteristics of earthquake surface ruptures: Issues and implications for seismic-hazard analysis and the process of earthquake rupture. *Bulletin of the Seismological Society of America* **98,** 1609-1632 (2008).

3. Field, E. H. *et al*. Uniform California Earthquake Rupture Forecast, Version 3 (UCERF3)—The Time-Independent Model. *Bulletin of the Seismological Society of America* **104,** 1122-1180 (2014).

4. Page, M. T., Field, E. H., Milner, K. R. & Powers, P. M. The UCERF3 grand inversion: Solving for the long-term rate of ruptures in a fault system. *Bulletin of the Seismological Society of America* **104,** 1181-1204 (2014).

5. Ambraseys, N. & Bilham, R. Earthquakes and associated deformation in northern Baluchistan 1892-2001. *Bulletin of the Seismological Society of America* **93,** 1573-1605 (2003).

6. Nakata, T., Otsuki, K. & Khan, S. H. Active faults, stress field and plate motion along the Indo-Eurasian plate boundary. *Tectonophysics* **181,** 83-95 (1990).

523 7. Haq, S. S. & Davis, D. M. Oblique convergence and the lobate mountain belts of western
524 Pakistan. *Geology* **25,** 23-26 (1997).
525 8. Sarwar, G. & DeJong, K. A. Arcs, oroclines, syntaxes: the curvature of mountain belts in
526 Pakistan. In *Geodynamics of Pakistan,* Geological Survey of Pakistan, 351-358 (1979).
527 9. Banks, C. J. & Warburton, J. 'Passive-roof'duplex geometry in the frontal structures of the
528 Kirthar and Sulaiman mountain belts, Pakistan. *Journal of Structural Geology* **8**, 229-237
529 (1986).
530 10. Humayon, M., Lillie, R. J. & Lawrence, R. D. Structural interpretation of the eastern
531 Sulaiman foldbelt and foredeep, Pakistan. *Tectonics* **10,** 299-324 (1991).
532 11. Davis, D. M. & Lillie, R. J. Changing mechanical response during continental collision: active
533 examples from the foreland thrust belts of Pakistan. *Journal of Structural Geology* **16,** 21-34
534 (1994).
535 12. Jadoon, I. A., Lawrence, R. D. & Shahid Hassan, K. Mari-Bugti pop-up zone in the central
536 Sulaiman fold belt, Pakistan. *Journal of Structural Geology* **16,** 147-158 (1994).
537 13. Bernard, M., Shen-Tu, B., Holt, W. E. & Davis, D. M. Kinematics of active deformation in the
538 Sulaiman Lobe and Range, Pakistan. *Journal of Geophysical Research* **105**, 13253-13279 (2000).
539 14. Copley, A. The formation of mountain range curvature by gravitational spreading. *Earth*
540 *and Planetary Science Letters* **351,** 208-214 (2012).
541 15. Reynolds, K., Copley, A. & Hussain, E. Evolution and dynamics of a fold-thrust belt: the
542 Sulaiman Range of Pakistan. *Geophysical Journal International* **201,** 683-710 (2015).
543 16. Macedo, J. & Marshak, S. Controls on the geometry of fold-thrust belt salients. *Geological*
544 *Society of America Bulletin* **111,** 1808-1822 (1999).

545 17. Wright, T. J., Lu, Z. & Wicks, C. Source model for the M_w 6.7, 23 October 2002, Nenana
546 Mountain Earthquake (Alaska) from InSAR. *Geophysical Research Letters* **30,** 1974 (2003).
547 18. Funning, G. J., Parsons, B., Wright, T. J., Jackson, J. A. & Fielding, E. J. Surface displacements
548 and source parameters of the 2003 Bam (Iran) earthquake from Envisat advanced synthetic
549 aperture radar imagery. *Journal of Geophysical Research* **110,** B09406 (2005).
550 19. Talebian, M. & Jackson, J. A reappraisal of earthquake focal mechanisms and active
551 shortening in the Zagros mountains of Iran. *Geophysical Journal International* **156**, 506-526
552 (2004).
553 20. Nissen, E., Tatar, M., Jackson, J. A. & Allen, M. B. New views on earthquake faulting in the
554 Zagros fold-and-thrust belt of Iran. *Geophysical Journal International* **186,** 928-944 (2011).
555 21. Satyabala, S. P., Yang, Z. & Bilham, R. Stick-slip advance of the Kohat Plateau in
556 Pakistan. *Nature Geoscience* **5,** 147-150 (2012).
557 22. Copley, A. & Reynolds, K. Imaging topographic growth by long-lived postseismic afterslip at
558 Sefidabeh, east Iran. *Tectonics* **33,** 330-345 (2014).
559 23. Ritzwoller, M. H., Shapiro, N. M., Levshin, A. L., Bergman, E. A. & Engdahl, E. R. Ability of a
560 global three-dimensional model to locate regional events. *Journal of Geophysical Research*
561 **108,** 2353 (2003).
562 24. Walker, R. T., Bergman, E. A., Szeliga, W. & Fielding, E. J. Insights into the 1968–1997
563 Dasht-e-Bayaz and Zirkuh earthquake sequences, eastern Iran, from calibrated relocations,
564 InSAR and high-resolution satellite imagery. *Geophysical Journal International* **187**, 1577-1603
565 (2011).

566 25. Szeliga, W., M. Historical and Modern Seismotectonics of the Indian Plate with an
567 Emphasis on its Western Boundary with the Eurasian Plate. *PhD thesis,* University of Colorado
568 (2010).
569 26. Pezzo, G., Boncori, J. P. M., Atzori, S., Antonioli, A. & Salvi, S.. Deformation of the western
570 Indian Plate boundary: insights from differential and multi-aperture InSAR data inversion for
571 the 2008 Baluchistan (Western Pakistan) seismic sequence. *Geophysical Journal*
572 *International* **198,** 25-39 (2014).
573 27. Pinel-Puysségur, B., Grandin, R., Bollinger, L. & Baudry, C. Multifaulting in a tectonic
574 syntaxis revealed by InSAR: The case of the Ziarat earthquake sequence (Pakistan). *Journal of*
575 *Geophysical Research* **119,** 5838-5854 (2014).
576 28. Molnar, P. & Lyon-Caen, H. Fault plane solutions of earthquakes and active tectonics of the
577 Tibetan Plateau and its margins. *Geophysical Journal International* **99,** 123-154. (1989).
578 29. Ishii, M., Shearer, P. M., Houston, H. & Vidale, J. E. Extent, duration and speed of the 2004
579 Sumatra–Andaman earthquake imaged by the Hi-Net array. *Nature* **435,** 933-936 (2005).
580 30. Trabant, C. *et al*. Data products at the IRIS DMC: stepping-stones for research and other
581 applications. *Seismological Research Letters* **83,** 846-854 (2012).
582 31. Stein, R. S. The role of stress transfer in earthquake occurrence. *Nature* **402,** 605-609
583 (1999).
584 32. Lin, J. & Stein, R. S. Stress triggering in thrust and subduction earthquakes and stress
585 interaction between the southern San Andreas and nearby thrust and strike-slip faults. *Journal*
586 *of Geophysical Research* **109,** B02303 (2004).

587 33. Tibi, R., Wiens, D. A., & Inoue, H. Remote triggering of deep earthquakes in the 2002 Tonga
588 sequences. *Nature* **424**, 921-925 (2003).
589 34. Hill, D. P. *et al*. Seismicity remotely triggered by the magnitude 7.3 Landers, California,
590 earthquake. *Science* **260,** 1617-1623 (1993).
591 35. Velasco, A. A., Hernandez, S., Parsons, T. & Pankow, K. Global ubiquity of dynamic
592 earthquake triggering. *Nature Geoscience* **1,** 375-379 (2008).
593 36. Pollitz, F. F., Stein, R. S., Sevilgen, V. & Bürgmann, R. The 11 April 2012 east Indian Ocean
594 earthquake triggered large aftershocks worldwide. *Nature* **490,** 250-253 (2012).
595 37. Lin, C. H. Remote triggering of the Mw 6.9 Hokkaido Earthquake as a Result of the Mw 6.6
596 Indonesian Earthquake on September 11, 2008. *Terrestrial, Atmospheric and Oceanic*
597 *Sciences* **23,** 283-290 (2012).
598 38. Voisin, C., Campillo, M., Ionescu, I. R., Cotton, F. & Scotti, O. Dynamic versus static stress
599 triggering and friction parameters: Inferences from the November 23, 1980, Irpinia
600 earthquake. *Journal of Geophysical Research: Solid Earth* **105,** 21647-21659 (2000).
601 39. Felzer, K. R. & Brodsky, E. E. (2006). Decay of aftershock density with distance indicates
602 triggering by dynamic stress. *Nature* **441,** 735-738.
603 40. Decriem, J. *et al*. The 2008 May 29 earthquake doublet in SW Iceland. *Geophysical Journal*
604 *International* **181,** 1128-1146 (2010).
605 41. Richards-Dinger, K., Stein, R. S. & Toda, S. Decay of aftershock density with distance does
606 not indicate triggering by dynamic stress. *Nature* **467,** 583-586 (2010).

42. Gomberg, J., Bodin, P. & Reasenberg, P. A. Observing earthquakes triggered in the near field by dynamic deformations. *Bulletin of the Seismological Society of America* **93,** 118-138 (2003).

43. Pollitz, F. F. & Johnston, M. J. Direct test of static stress versus dynamic stress triggering of aftershocks. *Geophysical Research Letters* **33,** L15318 (2006).

44. Parsons, T. & Velasco, A. A.. On near-source earthquake triggering. *Journal of Geophysical Research* **114,** B10307, (2009).

45. Harris, R. A. & Day, S. M. Dynamic 3D simulations of earthquakes on en echelon faults. *Geophysical Research Letters* **26,** 2089-2092 (1999).

46. Rubin, C. M. Systematic underestimation of earthquake magnitudes from large intracontinental reverse faults: Historical ruptures break across segment boundaries. *Geology* **24,** 989-992 (1996).

47. Meng, L. *et al*. Earthquake in a maze: Compressional rupture branching during the 2012 Mw 8.6 Sumatra earthquake. *Science* **337,** 724-726 (2012).

48. Dolan, J. F. *et al*. Prospects for Larger or More Frequent Earthquakes in the Los Angeles Metropolitan Region. *Science* **267,** 199-205 (1995).

49. Engdahl, E. R., van der Hilst, R. & Buland, R. Global teleseismic earthquake relocation with improved travel times and procedures for depth determination. *Bulletin of the Seismological Society of America* **88,** 722-743 (1998).

50. Argus, D. F. *et al*. The angular velocities of the plates and the velocity of Earth's centre from space geodesy. *Geophysical Journal International* **180**, 913-960 (2010).

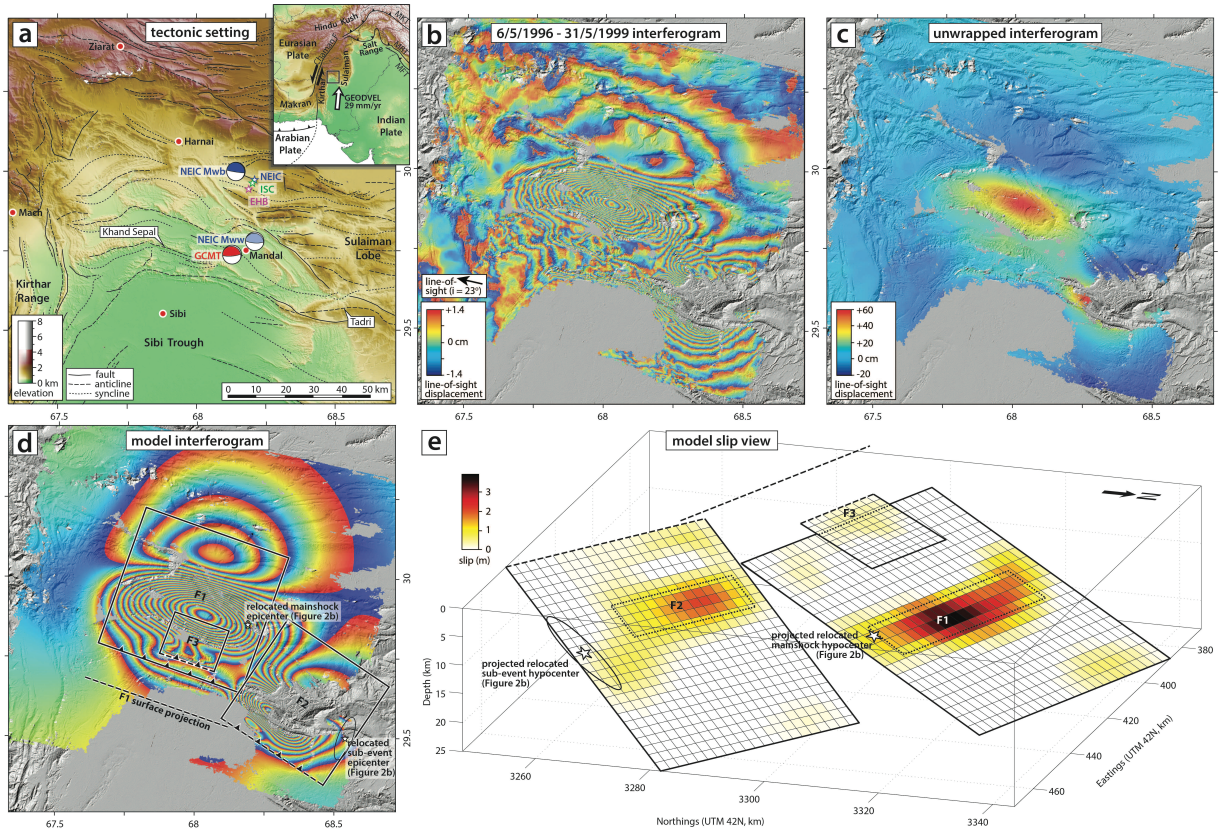

Figure 1 | Tectonic setting and InSAR observations and modelling. (a) Shaded topography of the study area with major surface faults and fold axes and published catalogue solutions for the 27 February 1997 Harnai earthquake. Earthquake epicentres are plotted from the United States Geological Survey's National Earthquake Information Center (NEIC, blue star), the International Seismological Centre (ISC, green star) and the Engdahl, van der Hilst & Bulland catalogue[49] (EHB, magenta star). Centroid moment tensors and centroid locations are shown from the Global Centroid Moment Tensor project (GCMT, red) and the NEIC *W*-phase project (NEIC-Mww, light blue). Finally a separate body-wave model from the NEIC is also plotted next to the NEIC epicenter (NEIC-Mwb, dark blue). Inset shows location within the western India–Eurasia collision zone, with arrow indicating the local velocity of the Indian Plate relative to Eurasia from the GEODVEL geodetic plate circuit model[50]. (b) ~3 year interferogram spanning the 27 February 1997 Harnai earthquake and its aftershocks, generated from ERS-2 descending track 091 scenes collected on 6 May 1996 and 31 May 1999 (orbits 5,456 and 21,488) with a 12 m perpendicular baseline. The line-of-sight incidence angle measured from the vertical is marked *i*. (c) Wrapped interferogram. (d) Model interferogram with model faults outlined in black and their up-dip surface projections marked by dashed lines. (e) Slip view with extents of the initial uniform slip faults indicated by dotted rectangles.

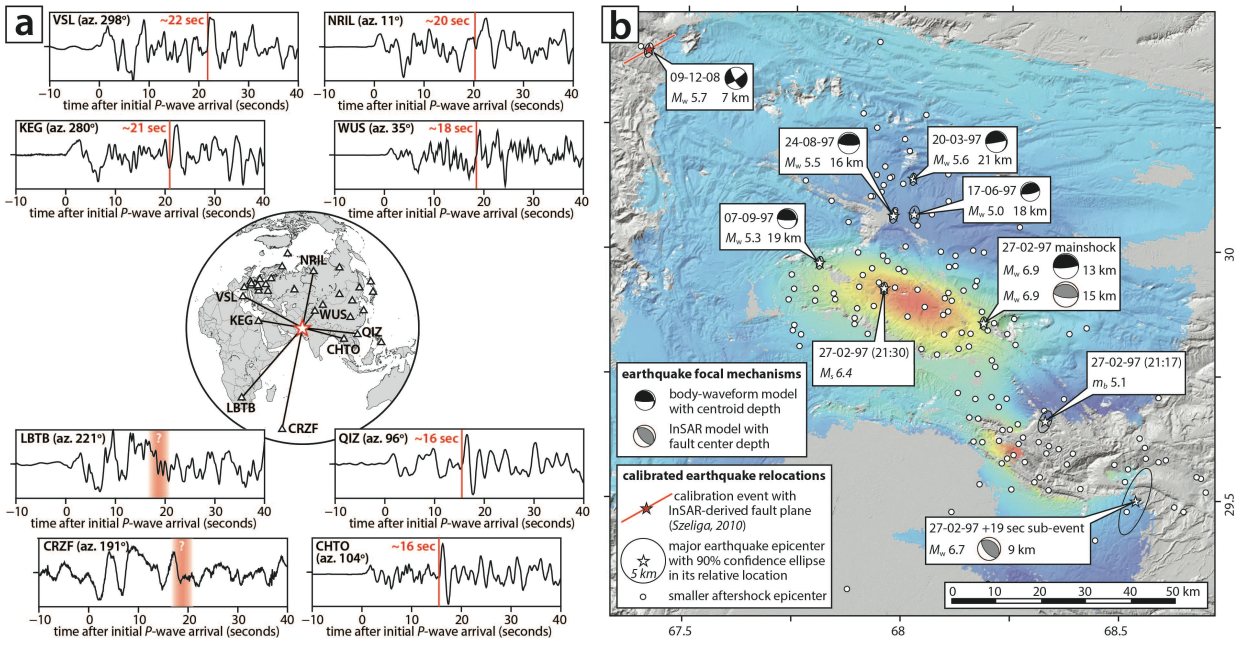

Figure 2 | Seismograms and relocated epicenters. (a) Eight broadband, vertical component seismograms of the Harnai earthquake, which demonstrate the azimuthal variation in delay between *P*-wave arrivals of the mainshock and those of the sub-event (red vertical line). Station locations and ray paths are plotted on the central map, along with additional stations used to relocate the sub-event epicentre. Stations LBTB and CRZF, at south-western azimuths, are not expected to show impulsive arrivals according to our InSAR-derived sub-event mechanism. (b) Calibrated epicentres for the Harnai mainshock, the +19 second sub-event, and 150 subsequent aftershocks, plotted over the unwrapped interferogram from Figure 1b. The largest aftershocks (M > 5.0) are represented by white stars with 90% confidence ellipses in their relative errors. Where available, focal mechanisms and centroid depths from body waveform or InSAR modelling are indicated. Smaller aftershocks are represented by white circles. To calibrate the entire cluster, we used an InSAR-derived fault model[25] for the 9 December 2008 Ziarat earthquake in the NW corner of the map[25-27] and assumed that its epicentre (red star) is positioned at the centre of this fault (red line). The body waveform solution for this event[25] is also shown.

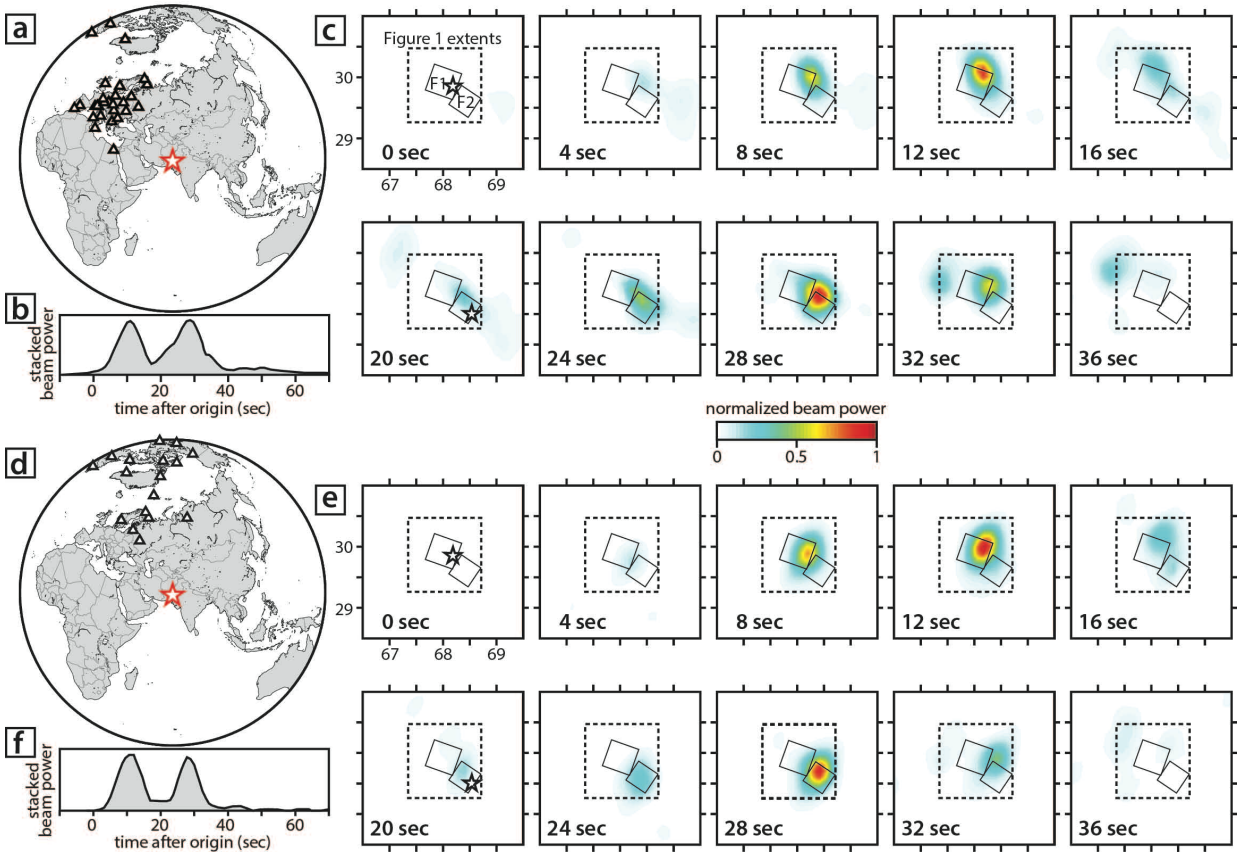

Figure 3 | Seismic back-projections. (a) Back-projection array constructed mostly from European seismic stations. (b) Normalized peak beam power stacked over all grid points. (c) Snapshots of coherent energy plotted at 4 second intervals after the initial rupture. For reference, the stars in the 0 second and 20 second plots indicate the relocated epicenters of the mainshock and +19 second sub-event, respectively (Figure 2b), while the small rectangles outline the F1 and F2 model faults (Figure 1d – e). (d) – (f) Back-projection from an array constructed mostly from North American stations, with details as in (a) – (c).

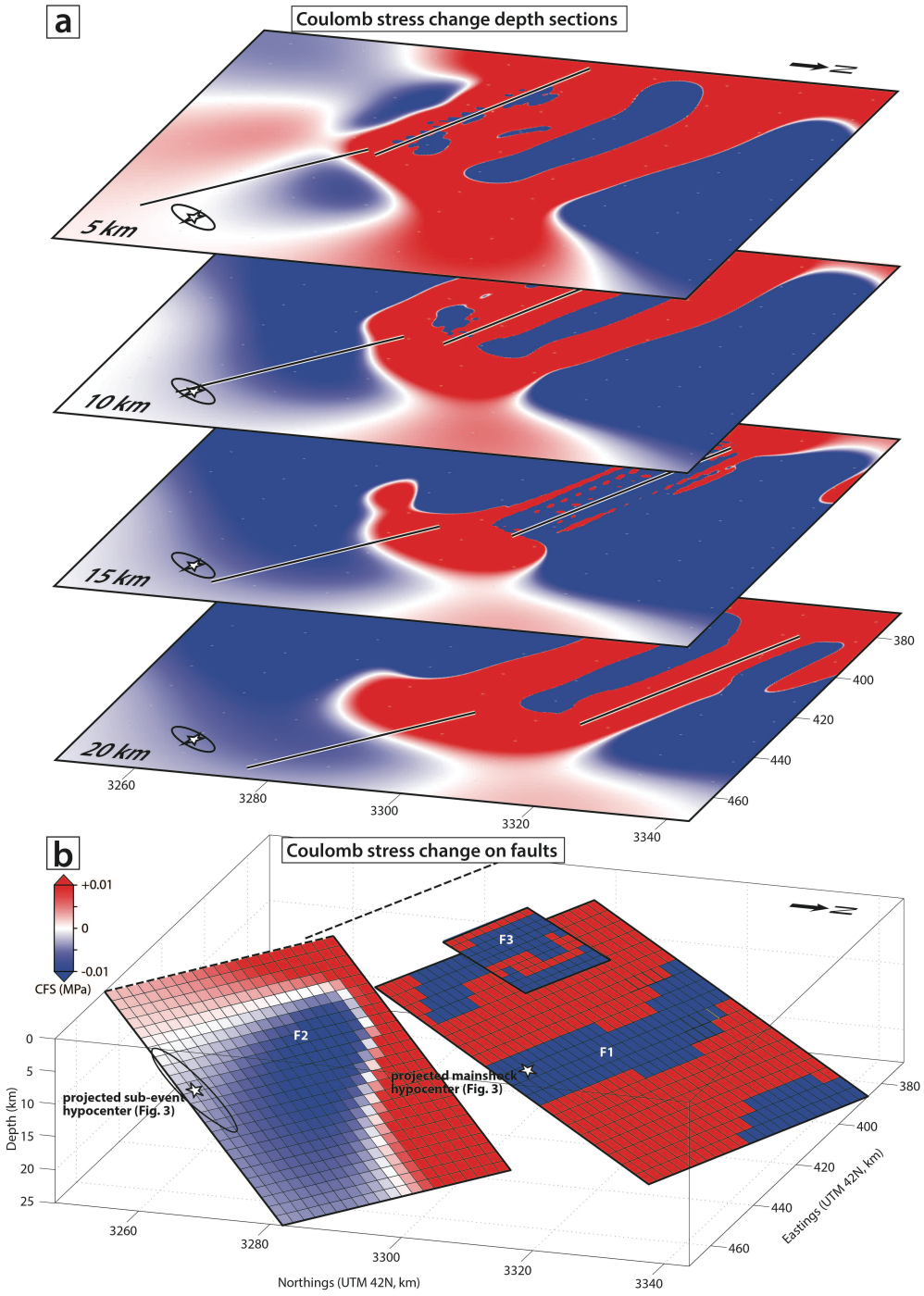

Figure 4 | Coulomb failure stresses. (a) Coulomb stress changes caused by slip on NE-dipping source fault F1 at 5 km depth intervals for receiver faults with the same orientation as F2. The sub-event epicenter is plotted with the 90% confidence ellipse in its relative location (Figure 2b); its hypocentre depth is probably 11 – 17 km. (b) Coulomb stress change resolved onto each receiver fault caused by slip on source fault F1.